Published in final edited form as:

Nat Neurosci. 2017 February ; 20(2): 189–199. doi:10.1038/nn.4467.

Developmental broadening of inhibitory sensory maps

Kathleen B Quast[1], **Kevin Ung**[2], **Emmanouil Froudarakis**[3], **Longwen Huang**[3], **Isabella Herman**[2,4], **Angela P Addison**[5,6], **Joshua Ortiz-Guzman**[2], **Keith Cordiner**[3], **Peter Saggau**[3,7], **Andreas S Tolias**[3,8], and **Benjamin R Arenkiel**[1,2,3,9]

[1]Department of Molecular & Human Genetics, Baylor College of Medicine, Houston, Texas, USA

[2]Program in Developmental Biology, Baylor College of Medicine, Houston, Texas, USA

[3]Department of Neuroscience, Baylor College of Medicine, Houston, Texas, USA

[4]Medical Scientist Training Program, Baylor College of Medicine, Houston, Texas, USA

[5]SMART Program, Baylor College of Medicine, Houston, Texas, USA

[6]University of St. Thomas, Houston, Texas, USA

[7]Allen Institute for Brain Science, Seattle, Washington, USA

[8]Department of Electrical and Computer Engineering, Rice University, Houston, Texas, USA

[9]Jan and Dan Duncan Neurological Research Institute at Texas Children's Hospital, Houston, Texas, USA

Abstract

Sensory maps are created by networks of neuronal responses that vary with their anatomical position, such that representations of the external world are systematically and topographically organized in the brain. Current understanding from studying excitatory maps is that maps are sculpted and refined throughout development and/or through sensory experience. Investigating the mouse olfactory bulb, where ongoing neurogenesis continually supplies new inhibitory granule cells into existing circuitry, we isolated the development of sensory maps formed by inhibitory networks. Using *in vivo* calcium imaging of odor responses, we compared functional responses of both maturing and established granule cells. We found that, in contrast to the refinement observed for excitatory maps, inhibitory sensory maps became broader with maturation. However, like excitatory maps, inhibitory sensory maps are sensitive to experience. These data describe the development of an inhibitory sensory map as a network, highlighting the differences from previously described excitatory maps.

Correspondence should be addressed to B.R.A. (arenkiel@bcm.edu).

AUTHOR CONTRIBUTIONS

K.B.Q. and B.R.A. designed the study, performed the analysis and wrote the manuscript. K.B.Q. performed most of the experiments. K.U. contributed to the behavior and wide-field imaging. E.F. and A.S.T. performed the two-photon experiments. L.H. performed the optogenetic mapping experiments on the AOD set up designed by L.H., K.C., P.S. and B.R.A. A.P.A., J.O.-G. and I.H. assisted with behavior, histology and surgeries.

COMPETING FINANCIAL INTERESTS

The authors declare no competing financial interests.

Understanding the relationship between structure and function in the brain requires investigating the full diversity of neuronal subtypes, and mapping their circuit connections. Traditional mapping techniques, such as lesions, anatomical tracing, fMRI, and intrinsic signal imaging, have been biased toward excitatory or mixed neuronal population responses. This is largely due to research that has historically focused on excitatory neuron responses, given that excitatory neurons in the cortex outnumber inhibitory neurons five to one[1]. Such maps have been instrumental in discerning the topographical organization and stereotyped response patterns of brain areas and have thus provided a general understanding of functional connectivity.

Maps are established and aligned via multiple mechanisms, including molecular cues, spontaneous or sensory-dependent remodeling, and refinement[2]. In the somatosensory cortex of rodents, excitatory thalamocortical afferents undergo activity-dependent refinement during a critical period of development[3]. Initially, somatosensory maps are diffuse and overlapping. With time, activity sculpts this diffuse pattern into refined barrels, such that individual whiskers are represented by discrete segments of cortex. Similar progression of map refinement occurs in many areas of the brain, including well-described processes in the visual system[4,5] and cerebellum[6,7]. Although our understanding of the functional relevance of sensory maps remains incomplete, general perception argues that they may serve critical roles in preserving sensory information or conveying computational advantages in the relay of afferent information to higher brain areas[8].

Genetic and imaging strategies now exist to selectively target diverse subtypes of neurons and allow monitoring of their functional connectivity[9,10]. These tools have revealed many properties of individual inhibitory neurons, as well as functional contributions of established inhibitory networks. Studies suggest that inhibitory interneurons respond to a wide variety of stimuli[11–13], provide blanket inhibition to surrounding neurons[14], and can regulate networks through the propagation of oscillations[15–17]. In sharp contrast to experience-dependent refinement of excitatory neuron responses, individual parvalbumin-positive interneurons in mouse visual cortex are initially narrowly tuned for orientation selectivity, but then become more broadly tuned[18]. However, mouse visual cortex lacks orientation-specific organization[19], and thus the developmental evolution of inhibitory network response properties, or maps, has remained elusive.

In this study, we used the mouse olfactory system to investigate the development of inhibitory neuron sensory maps. Inhibitory granule cells are the most numerous cell type in the olfactory bulb[20] and are continually added through postnatal neurogenesis and integrated into olfactory bulb circuits. Adult-born granule cells originate in the subventricular zone and migrate tangentially to the olfactory bulb, where they eventually populate the superficial granule cell layer and continue to mature anatomically, electrically and synaptically as they complete radial migration[21].

Unlike visual, auditory or other sensory modalities, the olfactory system detects discrete volatile stimuli from a large array of chemical molecules rather than a continuous sensory space. The olfactory bulb circuitry supports this segmentation of sensory space. Axons of olfactory sensory neurons that express in common an olfactory sensory receptor converge on

one or two glomeruli in the olfactory bulb[22–24]. Mitral and tufted cells receive sensory input from a single glomerulus and relay this information to the piriform cortex. Initial processing of sensory information occurs in the bulb, via input from local inhibitory interneurons onto mitral and tufted cells[25,26]. Thus, the spatially organized pattern of glomerular activation creates a sensory activation map specific to a given olfactory stimulus[27,28]. Initial experiments to dissect the structure and function of olfactory sensory maps examined either presynaptic sensory neuron projections[27] or intrinsic imaging responses of mixed cell populations[29,30]. More recently, higher resolution mapping techniques have defined response properties of specific neuronal subtypes from superficial interneurons in the glomerular layer of the bulb[31]. It remains unknown, however, how the vast inhibitory interneuron network in the granule cell layer dynamically contributes to olfactory sensory mapping.

Here we investigated the development of inhibitory interneuron sensory maps. We use the term “map” as a way to describe discrete activation domains to different odorants, whereby we have mapped the area (size and position) of the olfactory bulb’s inhibitory network upon activation by several different specific olfactory stimuli. We used viral delivery of conditional GCaMP6 into olfactory bulbs of either *Dlx5/6-Cre* or *Crhr1-Cre* mice, which genetically targets expression of this calcium indicator to early-stage or mature granule cells, respectively. We tracked the development of sensory maps of inhibitory granule cells during their integration into olfactory bulb circuitry and found that single odors produced broader sensory maps from mature integrated inhibitory cells than from immature, developing inhibitory cells. We further found that these maps were sensitive to experience manipulations and that olfactory-driven learning precociously expanded network responses, while blocking sensory experience restricted maps to an immature state. In summary, we describe the formation and expansion of an inhibitory sensory network map *in vivo*. This developmental broadening of an inhibitory sensory network contrasts sharply with previously described excitatory map pruning and refinement, but simultaneously exhibits the shared property of experience-dependent plasticity.

RESULTS

Genetic labeling of inhibitory granule cells at differing maturation states

With the goal of mapping sensory activation in developmental subsets of inhibitory interneurons within the olfactory bulb, we implemented conditional viral genetic methods to selectively label granule cells at different stages of maturation. We used transgenic mice that expressed Cre recombinase under the control of a promoter from either the inhibitory progenitor marker Dlx5/6 (ref. 32), to target immature adult-born granule cells, or corticotropin-releasing hormone receptor (Crhr1), which marks mature, integrated granule cells[33]. Using conditional viral reporters, we verified that both Cre lines labeled granule cells (Fig. 1a,b), but whereas GFP-labeled cells were concentrated in the middle or deep layers of Dlx5/6-Cre bulbs, Crhr1-targeted cells were predominantly located near the superficial and middle granule cell layers (Fig. 1a). This is consistent with granule cell migration patterns whereby early progenitors migrate from the core of the olfactory bulb to the superficial layer, which is enriched in mature and integrated granule cells[21,34].

In addition to the temporal specification provided by conditional viral labeling, we also spatially limited the injection to the center of the olfactory bulb, thereby avoiding neuroblasts in the rostral migratory stream and other layers of the olfactory bulb where inhibitory neurons reside. Thus, the vast majority of the cells labeled through conditional viral injections were granule cells, and we rarely observed labeled cells outside the granule cell layer in either Dlx5/6-Cre or Crhr1-Cre targeted mice (Fig. 1a).

To differentiate the temporal dynamics of the Dlx5/6 and Crhr1 drivers in the olfactory bulb, we performed 5-ethynyl-2′-deoxyuridine (EdU) birth dating in combination with viral labeling. Dlx5/6-Cre mice were first pulsed with the proliferation marker EdU, followed by injections of conditional GFP virus into the olfactory bulb at time points ranging between 7 and 60 d after EdU delivery (Fig. 1c,d top). At the earliest time points examined, 7 and 14 d after EdU labeling, we observed the highest ratio of GFP^+EdU^+/total EdU^+ cells, whereas the amount of coexpression dropped below half of the highest ratio after 21 d, eventually plateauing by 40 d (Fig. 1c,e). By targeting viral delivery to the olfactory bulb and avoiding brain structures that harbor earlier-stage granule cell progenitors, we never observed co-labeling ratios above 60% at the earliest time points, when many migrating neurons have not reached the olfactory bulb. Notably, and integral to our study design, this developmental expression pattern was the inverse of what we previously obtained for the temporal expression in Crhr1-expressing neurons[33] (Fig. 1c bottom and Fig. 1e), where we noted colabeling in more than 50% of new granule cells 21 d after EdU labeling and where the ratio plateaued to near 100% by 28 d. Thus, using the Dlx5/6-Cre and Crhr1-Cre driver lines, combined with stereotaxic viral injections of conditional reporters into the core of the olfactory bulb, we isolated granule cells at distinct stages of interneuron development.

Functional maturation states of genetically labeled granule cells

We next sought to determine the functional maturation state of selectively labeled inhibitory granule cells via whole-cell patch clamp electrophysiology. Through visually targeted whole-cell recordings, we found that both Dlx5/6- and Crhr1-expressing neurons were active, and injected current elicited action potentials (Fig. 2a). However, although Dlx5/6-expressing neurons were electrically functional, they displayed several indicators of a more immature state, including wider action potential half-width (2.691 ± 0.23 ms versus 2.02 ± 0.19 ms), higher membrane resistance (970 ± 79 MΩ versus 645 ± 57 MΩ) and lower capacitance (11.43 ± 0.82 pF versus 13.71 ± 1.28 pF) (Fig. 2b–d). However, we did not observe any differences between the two classes of granule cells in the frequency–current curves, resting potentials, amount of current needed to reach action potential threshold (14.91 ± 1.78 pA versus 18.56 ± 2.87 pA) or time to action potential peak in response to a current injection (49.05 ± 7.00 ms versus 62.74.70 ± 11.36 ms at 30pA) (Fig. 2e–h). In fact, anatomically we did not observe gross morphological differences between these developmentally staggered groups of granule cells (Supplementary Fig. 1).

To distinguish whether Dlx5/6-expressing cells are early stage neurons that later give rise to Crhr1-expressing neurons, versus a distinct neuronal subpopulation, we crossed Dlx5/6-Cre mice to Crhr1-GFP reporter mice and virally labeled Dlx5/6-expressing cells to track the conversion of Dlx5/6 neurons into Crhr1 neurons over time (Fig. 2i). We observed only a

small overlap in the labeled cells 14 d after viral injection of AAV-flex-tdTomato to label Dlx5/6 neurons, whereas the percentage of original Dlx5/6-expressing cells that became Crhr1^{+} increased to over 80% by 60 d after injection (Fig. 2j,k). Together, these data suggest that the two drivers label functionally distinct stages of granule cell development, but both types of cells respond and fire action potentials similarly to presynaptic excitatory input, and both populations could actively participate in olfactory bulb circuitry.

Sensory maps of the olfactory bulb

Having established the genetic tools to label granule cells at distinct stages of maturation, we next sought to compare sensory-evoked spatial activation patterns formed by these interneuron networks. Toward this end, we targeted expression of the genetically encoded calcium indicator GCaMP to either Dlx5/6- or Crhr1-expressing granule cells and performed wide-field epifluorescence calcium imaging. We did not observe any evidence that expression of GCaMP changed the development of targeted cells, as there were no appreciable differences in intrinsic membrane properties of Dlx5/6 neurons after 2 weeks of viral GFP or GCaMP6m expression (Supplementary Fig. 2). We then recorded population-level sensory activation of inhibitory neuron networks at discrete stages of maturation by visualizing the entire dorsal olfactory bulb through thinned skulls of anesthetized animals expressing GCaMP variants (Fig. 3a).

To establish a reference excitatory odor map against which to compare developing inhibitory odor maps, we first examined the sensory odor response maps of mitral and tufted cells in the glomerular layer of Thy1-GCaMP3 transgenic reporter mice[35] (Fig. 3a–c). To evaluate the specificity of responses, we differentially presented a panel of 12 odorants, each of which activated a different set of glomeruli (Fig. 3c and data not shown). Although the precise activation patterns varied slightly between animals, the general area of activation was consistent and reproducible. Previous studies that implemented either intrinsic signal imaging[29,30], imaging of synapto-pHluorin release from presynaptic olfactory sensory neuron terminals[27] or mitral cell calcium imaging[35] produced similar olfactory sensory maps in the olfactory bulb.

We next targeted maturing granule cells for GCaMP expression and odor response mapping. Conditional viral expression of the genetically encoded calcium indicator GCaMP6m[36] in Dlx5/6-Cre or Crhr1-Cre mice allowed us to differentially detect the activation of populations of granule cells as a change in fluorescence of the dendrites in the external plexiform layer of the olfactory bub. Initially examining immature, Dlx5/6-expressing granule cells, we noted larger contiguous areas of activation than we observed from the mitral and tufted cell imaging (areas spanning several glomeruli) (Fig. 3d). This responsive area was located in a similar position to the activated mitral and tufted cells observed in Thy1-GCaMP3 mice and dynamically changed in accordance with the stimulus presented. However, unlike mitral and tufted cells, the apical dendrites of granule cells are not anatomically restricted to a single glomerulus, thus we did not see evidence of specific glomerular-type response, but instead observed larger, more diffuse activation patterns that were qualitatively distinct. The differentially activated areas were stimulus-specific and not a result of the viral labeling or imaging procedure, since the maps reported odor-specific

activation patterns across the entire dorsal surface of the bulb and were contingent upon the stimulus. Together, these data allowed us to begin to construct inhibitory network maps that largely paralleled excitatory mitral cell activation domains, albeit with qualitatively different and more diffuse areas.

Inhibitory sensory maps become broader with maturation

After elucidating the sensory maps of immature granule cells, we next constructed maps for more mature granule networks using the Crhr1-Cre driver line. Hypothesizing that inhibitory maps, like their excitatory counterparts, are pruned and refined as circuits mature, we expected sharpening in mature granule cell sensory maps. Instead, we observed that a given odorant activated Crhr1-expressing granule cells across wider areas of the bulb than Dlx5/6-expressing granule cells (Fig. 3e). To quantify the area activated by a specific stimulus, we set the threshold for response maps at 50% maximal change in fluorescence (ΔF) (Fig. 4a–c) and compared the centroid of the activated area for each cell type. We found that overlapping activated areas across cell types were dynamic for the stimulus presented (Fig. 4d). When we compared the consensus maps from multiple animals for the odorant pentanol, we noted that the Dlx5/6 map was smaller in area than the Crhr1 map, but the overall positioning was consistent (Fig. 4e). We analyzed both ΔF (Fig. 4) and the ratiometric change in fluorescence ($\Delta F/F$) (Supplementary Fig. 3). Maximal ΔF and $\Delta F/F$ values were similar for the two populations of granule cells (Fig. 4f and Supplementary Fig. 3c), suggesting that neither the maximum density of the activated cells nor the GCaMP6 viral expression was noticeably different in the two granule cell populations. We report the ΔF analysis to remain consistent with olfactory bulb response maps described previously[27,31]. The area activated by pentanol (area ≥ 50% of the maximal ΔF response) showed significantly larger domains for the mature Crhr1-expressing granule cells compared to immature Dlx5/6-expressing cells, occupying more than twice the area (Fig. 4b,c,g). In addition to analyzing activated areas, we also compared normalized fluorescence values for all pixels in the non-thresholded response maps, observing a right shift toward increased proportion of higher ΔF values in the mature Crhr1 labeled granule cells (Fig. 4h). After analyzing other odorants in a similar manner, we found a comparable activated area expansion in mature granule cells versus younger ones across stimuli (Supplementary Fig. 4). Thus the observed broadening of inhibitory sensory maps with developmental maturation, without obvious changes in maximal fluorescence levels, suggested that mature granule cells receive more inputs[37–39].

Finally, to validate that Dlx5/6-targeted neurons follow the same developmental trajectory as Crhr1-expressing neurons, we conducted mapping experiments in Dlx5/6-Cre animals at later time points. For this, we again targeted Dlx5/6-expressing neurons for GCaMP6m expression, but waited 5–6 weeks after viral labeling to allow the granule cells to fully mature before imaging. Like Crhr1 maps, Dlx5/6 maps generated 5–6 weeks after injection had larger activated areas than those of the immature Dlx5/6-expressing population (Supplementary Fig. 5). Together, these data suggest that the observed inhibitory network map expansion is due to the maturation state of the granule cells and not differential targeting of conditional GCaMP reporters to different granule cell subtypes.

Additional excitatory inputs with inhibitory map expansion

Having described the developmental broadening of granule cell sensory maps, we next sought synaptic evidence of additional inputs. We reasoned that if distant mitral cells can more effectively activate mature granule cells, we might expect that mature granule cells would receive additional and/or more diverse excitatory synapses. Using whole cell recordings, we assayed the synaptic inputs onto the two different populations of granule cells by recording miniature excitatory postsynaptic currents (mEPSCs) (Fig. 5a). Consistent with anticipated connectivity changes that are thought to occur with neuronal maturation, we measured significantly more excitatory synaptic events in Crhr1-expressing cells than in Dlx5/6-expressing ones (Dlx5/6-Cre mEPSC frequency 0.231 ± 0.057 Hz, Crhr1-Cre mEPSC frequency 1.199 ± 0.297 Hz) (Fig. 5b), indicating the presence of enhanced synaptic connectivity in the more mature cohort. There was no change in the mean cell mEPSC amplitude (Dlx5/6-Cre mEPSC amplitude 1.49 ± 0.15 pA, Crhr1-Cre mEPSC amplitude 1.757 ± 0.1874 pA) (Fig. 5c inset), but we did note a significant difference in the variance of all the events in the cells measured (Fig. 5c). Thus, mature Crhr1-expressing cells receive more synapses than immature Dlx5/6-expressing cells.

To further confirm that granule cells add inputs from distal mitral cell as they mature, we implemented optogenetic mapping to measure functional connections from channelrhodopsin (ChR2)-expressing mitral cells onto either immature or mature granule cells (Fig. 5d–f)[40]. By limiting blue light to a small, 30-μm-diameter area of illumination (Supplementary Fig. 6), we activated either proximal or distal mitral cells and measured the synaptic input onto either immature or mature neurons (Dlx5/6-Cre neurons 2–3 or 5–6 weeks after viral injection, respectively) (Fig. 5d–f). We found that mature granule cells received stronger connections from distal mitral cells, whereas immature granule cells received little to no input from mitral cells further than 250 μm away (the approximate radius of the immature sensory activated maps) (Fig. 5f). Thus the expansion of the granule cell map is at least in part due to increased connections from distal mitral cells.

Individual granule cells become broadly tuned

We noted that, as a network, granule cell response areas became larger with maturation, but we also sought to explore the response properties of individual granule cells *in vivo*. Toward this end we visualized calcium transients by two-photon imaging in both mature and immature granule cells in response to a small panel of odorants (Fig. 6a,b). We found that mature neurons were more likely to respond to odor stimulation than immature neurons (26.3% Dlx5/6-expressing neurons responding versus 50.6% Crhr1-expressing neurons responding) (Fig. 6c top). Of the responsive granule cells, we found that the Dlx5/6-targeted cohort overwhelmingly responded to a single odor (Fig. 6c bottom) whereas Crhr1-targeted neurons responded to a broader range of stimuli. Whereas only 12.6% of the responsive Dlx5/6 neurons responded to multiple odors, 38.1% of Crhr1 neurons did so. Moreover, a small percentage of this more mature population responded to four or more odors. When we evaluated profiles to individual odors, we found that, of the responsive neurons, a similar percentage of the Dlx5/6 neurons responded to each of the different olfactory stimuli presented, including complex odors such as coffee and a mixture of eight individual chemicals, whereas significantly more Crhr1 neurons responded to the complex odorants

(Fig. 6d). Thus, not only do sensory maps of granule cell networks become larger and broader with development, the tuning properties of individual granule cells become both more responsive and more broadly tuned as well.

Developing granule cell maps are susceptible to experience manipulations

A hallmark of developing excitatory sensory maps is susceptibility to experience or activity manipulations. To test whether inhibitory maps are likewise sensitive, we performed two different manipulations of the animals' sensory experience. First we wanted to determine how restricting sensory experience might affect normal granule cell map maturation. To test this, we performed unilateral, reversible naris occlusion[41] for 5–6 weeks in mice that expressed GCaMP in either immature (Dlx5/6) or mature (Crhr1) granule cells (Fig. 7a,b). Comparing the sensory maps of the occluded to the open control side (Fig. 7c,d), we found that decreased sensory experience prevented normal expansion of immature granule cell sensory maps (Fig. 7e), but had no effect on the sensory maps of the mature granule cells (Fig. 7f). Furthermore, the maximal ΔF did not change in either state. To determine whether this sensory manipulation resulted in synaptic changes, we performed whole-cell mEPSC analysis in both sets of neurons (Fig. 7g–k). We found a sharp and significant decrease in the frequency of events only in the immature cells (Fig. 7h,i), whereas more mature cells showed no change, suggesting that once established the number of synaptic connections onto granule cells is stable.

As decreased sensory experience prevented the expansion of inhibitory sensory maps, we next enhanced olfactory sensory experience by training mice in a Go/NoGo olfactory task (Fig. 8a). After habituating the mice to a training box, we labeled immature granule cells with the GCaMP virus and trained the mice to perform a Go/NoGo task (Fig. 8b and Supplementary Fig. 7a). We next imaged GCaMP response maps to the odorants used in the training (Fig. 8c) and analyzed the activation domains as described previously (Fig. 4). Compared to that in control mice that were not trained, the area of the bulb activated by the trained odors was significantly larger (Fig. 8d). The data suggest that this premature expansion of the sensory map was specific to the trained odors, since novel odors did not elicit a similar expansion. This effect was not due to the odor selected for training, as different odor pairs produced similar results (Supplementary Fig. 7b,c). Recording the synaptic events after training showed increased variability of event frequency (Supplementary Fig. 7d–f), with a trend toward increased event frequency. This is not surprising, since interneuron map expansion was specific to the training odors and responses are sparse to individual odors. Together, these data suggest that learning resulted in map expansion, as both rewarded and unrewarded odor maps were plastic and repeated passive exposure to odors without learning did not cause map expansion (Supplementary Fig. 8). Additionally, learning-induced sensory map expansion was limited to immature neurons, given that training and subsequent imaging of mature granule cells did not change either activation domains or synaptic properties (Supplementary Fig. 9). Thus, our findings support a model whereby developing granule cells may initially receive centralized connections located near the activated mitral cells, and with sensory experience (or normal maturation) they may receive additional inputs from distal mitral cells to expand the inhibitory sensory map (Fig. 8e,f).

DISCUSSION

By genetically targeting different stages of granule cell maturation for temporally defined and cell type–specific expression of GCaMP6, we have begun to reveal the development of sensory maps in an inhibitory network. Combining genetic, viral and *in vivo* imaging methods, we were able to isolate and monitor the activity of inhibitory interneuron populations as they become integrated into existing excitatory circuitry and further analyze how functional integration translates into sensory activation of a network. Notably, we found that, in contrast to previously described maps that show consolidation and refinement of excitatory connections with maturation, interneurons display a dramatic expansion and broadening of their patterned connectivity. Although excitatory and inhibitory cells have opposing functions in the brain, and as such it is reasonable that their network development would likewise be different, it is still surprising that inhibitory sensory map development was opposite.

Historically, granule cell function has been closely tied to lateral inhibition and contrast enhancement[42]. Although the dendrites of individual granule cells extend only 200 μm within the external plexiform layer, the lateral dendrites of mitral cells can reach over 1,000 μm and are thought to connect distant areas of the olfactory bulb[20]. Consistent with this, our data suggest that granule cells are first innervated by common or local inputs before being recruited by distant, functionally distinct areas.

Intriguingly, map expansion evident in olfactory bulb granule cells may be a fundamental principle of inhibitory map development. If most inhibitory cells are broadly tuned or can respond to a wide range of stimuli, it would follow that an individual stimulus could activate a diverse and expansive number of inhibitory cells, thereby creating a broad map. Such a broad map could either be present from the earliest stages of development or, as we found, the map could evolve and broaden through experience and time. These types of associative connections that result from adding distal inputs after the establishment of initial local connections are ideal cellular candidates for brain state-dependent neuromodulation, learning, or memory.

Current theories on the importance of granule cells have suggested roles in plasticity and memory. Likewise, the importance of inhibitory neurons in brain plasticity is well supported. Previously, the search for neural correlates of learning and plasticity had focused largely on excitatory cells and synapses, but it is now appreciated that inhibitory interneurons also play an integral role in the brain's ability to adapt and learn. Inhibitory neurons directly influence phases of enhanced plasticity during critical periods[43], and inhibitory circuits contribute to both acquisition and expression of fear conditioning memory[44]. Thus, it is vital to better understand the developmental mechanisms that govern inhibitory network sensory map formation and function and to elucidate the contributions of inhibitory networks toward sensory processing.

Inhibitory input by adult-born granule cells in the olfactory circuit is a critical determinant of odor detection threshold, short-term olfactory memory and perceptual learning[45–47]. In turn, olfactory learning itself can increase granule cell survival[48,49], demonstrating a

dynamic and intricate relationship between learning, circuit maintenance and granule cell function. Our findings that experience and learning can enhance inhibitory sensory map development support the importance of inhibitory cells in these behaviors. Granule cells initially receive excitatory inputs onto their somata and basal dendrites before they receive excitatory inputs on their distal dendrites[37–39]. These initial inputs may originate from local mitral cells and centrifugal inputs, whereas additional connectivity later in their development might come from distant mitral cells. Thus, immature inhibitory sensory maps may provide contextual information for early sensory processing, which is later modulated by activity-dependent synaptogenesis. One intriguing possible biological consequence of this is that developmental expansion of inhibitory sensory maps may represent circuit substrates for associative learning.

We have also defined the later stages of granule cell maturation based on molecular markers instead of relying strictly on birth-dating. By focusing on genetic markers, we were able to differentiate late-developing granule cells from the mature, fully integrated cells and thus detect the different functions they may have in sensory processing and/or learning. Altogether, we describe here the formation and expansion of an inhibitory sensory network map *in vivo*, as well as the sensitivity of inhibitory sensory maps to experience manipulations. Further, we highlight the marked differences in map expansion versus refinement of interneurons compared to excitatory cells during development. With these data, it now becomes intuitive that interneuron sensory maps show this type of map expansion with maturation, since the main role for interneurons is to act as the refinement regulator of excitatory circuits. Overall, our mapping efforts have both revealed potential general principles of interneuron network development and reinforced the importance of examining multiple cell types toward better understanding how differential cell types and their patterns of functional connectivity contribute to brain function.

ONLINE METHODS

Experimental animals

All experimental animals were treated in compliance with the US Department of Health and Human Services and Baylor College of Medicine IACUC guidelines. *Crhr1-Cre* (ref. 9), *Dlx5/6-Cre* (ref. 50), *Crhr1-EGFP* (ref. 51), *Thy1-ChR2* (ref. 52) and *Thy1-GCaMP3* (ref. 35) mice were previously described. All experiments were performed on mice of both sexes ages 7–14 weeks.

Viral injection and edU pulsing

Adeno-associated viruses (AAV) serotype DJ/8 encoding flexed-GCaMP6m[36], flexed-GFP or flexed-tdTomato were packaged in house. 630 nL AAV (~2.5×10^{12} viral particles/mL) were injected into the main olfactory bulb (from bregma: ML, ± 0.9 mm; AP, 3.82 mm; and 0.9 mm from the surface of the bulb) of Dlx5/6-Cre or Crhr1-Cre mice using glass injection pipettes and a Nanoject II (Drummond Scientific Company, Broomall, PA) with a rate of 63 nL/s at 20-s intervals to obtain uniform labeling of granule cells.

Birth-dating of neurons was performed as previously described[33]. Briefly, adult Dlx5/6-Cre or Crhr1-Cre mice received two doses of EdU (Invitrogen, 50 mg/kg) intraperitoneally 8 h apart. Seven, 14, 21, 28, 45 and 60 d after EdU pulsing, AAV-flex-GFP was injected into the Dlx5/6-Cre olfactory bulb as described above, and experimental mice were sacrificed 14 d after injection for imaging and colocalization analysis.

Immunohistochemistry and confocal imaging

For confocal imaging, animals were deeply anesthetized using isoflurane, followed by intracardial perfusion of PBS and 4% PFA. Brains were dissected, postfixed in 4% PFA at 4 °C overnight before cryoprotection in 30% sucrose. Olfactory bulbs were coronally sectioned at 25 μm using a cryostat (CM1860, Leica). Free-floating sections were stained with rabbit anti-GFP (Synaptic Systems, Cat. No. 132 003, 1:1,000) and a Click-iT EdU Alexa-555 kit (Invitrogen C10338) and anti-rabbit Alexa-488 (1:500 Invitrogen A32731). Confocal images were obtained using a Leica TCS SPE confocal microscope. Single optical planes were imaged with a 20× objective. The field of view spanned all layers of the granule cell area. For birthdating assays, the total number of EdU-546 positive cells and number of GFP cells colocalizing with EdU-546 were counted blind to time point. For the timeframe for maturation of Dlx5/6 cells into CHRH cells, the total number of AAV-flex-tdTomato cells and number of AAV-flex-tdTomato cells colocalizing with Crhr1-GFP were counted blind.

Anatomic reconstructions of single cells were assessed from animals injected with low titer AAV-flex-GFP virus. 80-μm horizontal sections were stained with rabbit anti-GFP (Synaptic Systems, 1:1,000) and subsequently anti-rabbit Alexa-488 (1:500). Confocal *z*-stacks were obtained at 1-μm intervals covering the entire cell. Only cells without any clipping of dendritic arbors were analyzed. Analysis was performed blind to genotype, and granule cells were reconstructed using Neurolucida Software (MBF Bioscience, Williston, VT).

Electrophysiology

Mice were deeply anesthetized with isoflurane and then perfused with cold artificial cerebrospinal fluid (ACSF, in mM:125 NaCl, 25 glucose, 25 $NaHCO_3$, 2.5 KCl, 2 $CaCl_2$, 1.25 NaH_2PO_4 and 1 $MgCl_2$, pH 7.3, 310–320 mOsm). The brain was dissected, embedded in low melting point agarose and placed in an ice-cold sucrose-based cutting solution (in mM: 87 NaCl, 2.5 KCl, 1.6 NaH_2PO_4, 25 $NaHCO_3$, 75 sucrose, 10 glucose, 1.3 ascorbic acid, 0.5 $CaCl_2$, 7 $MgCl_2$). 300-μm-thick coronal olfactory bulb slices were sectioned on a vibratome (VT1200, Leica). Slices were then recovered in oxygenated ACSF (37 °C) for 15 min and allowed to acclimate to room temperature for at least 15 min before recordings.

Granule cells were targeted using a combination of infrared Nomarski DIC optics and fluorescence microscopy (BX50WI, Olympus) and further identified by their high input resistance. Recordings were obtained on an Axon MultiClamp 700B amplifier and digitized at 10 kHz (Axon Digidata 1440A). Recording electrodes (5–8 MΩ) were fabricated from borosilicate glass microcapillaries (outer diameter, 1.5 mm) with a micropipette puller (Sutter Instruments).

Miniature excitatory postsynaptic currents (mEPSCs) were recorded from GFP^+ or $tdTomato^+$ granule cells in oxygenated ACSF containing 1 μM TTX, 10 μM APV, 20 μM bicuculline, using an internal solution that contained (in mM) 120 cesium methanesulfonate, 6 CsCl, 2 $MgCl_2$, 0.05 $CaCl_2$, 20 HEPES, 0.02 EGTA, 10 phosphocreatine disodium salt, 4 Mg-ATP, 0.4 Na_3-GTP, 0.2% biocytin (pH 7.2 with CsOH, 290–300 mOsm). Cells were held at -70 mV throughout the experiment and access resistances were maintained at less than 30 MΩ. Signals were low pass filtered at 2 kHz and analyzed using MiniAnalysis (Synaptosoft) blind to cell type. mEPSC recordings for naris occlusion manipulations were performed after injecting AAV-flex-GFP in the right bulb and AAV-flex-tdTomato in the left bulb, randomly inserting the nose plug and performing the recordings blind to the occluded side.

Intrinsic membrane and spiking properties were recorded from GFP^+ granule cells in oxygenated ACSF using an internal solution that contained (in mM) 120 potassium gluconate, 10 KCl, 10 phosphocreatine, 4 Mg-ATP, 0.3 Na-GTP, 10 HEPES and 0.15% biocytin (pH 7.3, 290–300 mOsm). Resting potential and compensated input resistance was recorded within seconds of breaking into a cell. Cells with a series resistance of <30 MΩ and <25% change for the duration of the experiment were used for analysis. Analysis of current-clamp electrophysiological data was performed using pClamp10 (Molecular Devices) Single action potential parameters (peak amplitude, half-width and hyperpolarization anti-peak) were measured at threshold and action potential amplitudes and after-hyperpolarization potentials were measured relative to action potential threshold. To measure granule cell firing properties, the frequency–current relationship was calculated as the spike frequency after current steps from 0 pA (resting approximately −60 mV) to 100 pA were applied in increments of 10 pA (0.05 Hz, 1,000 ms duration).

Optogenetic mapping of mitral cell inputs onto GCs were performed on *Thy1-ChR2; Dlx5/6-Cre* mice injected with AAV-flex-tdTomato. Recordings occurred either 2 weeks after injections (immature GCs) or 5–6 weeks after injections (mature GCs). An acousto-optic deflector (AOD)-based microscope system was used to optically stimulate the ChR2-expressing mitral cells. A BLM-Series 473 nm blue laser system (Spectra Services) was used to generate laser beams. A neutral density filter (Thorlabs) was used to attenuate laser intensity. Two orthogonally mounted AODs (LS55-V, Isomet) were employed to produce an arbitrary random-access 2D scan pattern. To generate acoustic waves for deflectors, two deflector drivers (IntraAction Corp.) were implemented. Custom software in Matlab (MathWorks) controlling output voltages through a D/A converter (National Instruments) connected the deflector drivers. A scan angle magnification telescope was used to increase scan range to fit the objective's field of view. Finally, the AOD scanning beam was coupled into the upright microscope. For circuit mapping, stimulation sites were programmed at grid points spaced 30 μm along the mitral cell layer in coronal olfactory bulb slices with 15 ms duration and 1 s intervals. To elicit action potentials in $ChR2^+$ cells from the Thy1-ChR2 mice with high fidelity and spatiotemporal resolution, we optimized the laser intensity (40 mW/mm^2). For connectivity mapping experiments, we considered a synaptic event as an evoked postsynaptic current if it met two criteria: the amplitude was over 5 pA and the onset of the PSC was within 20 ms after the onset of laser stimulation. Each trace was analyzed, and the evoked PSC amplitude and probability for each stimulation spot were calculated.

Calcium imaging

In vivo wide-field calcium imaging was performed in anesthetized (urethane, 1.2 μg/kg) head-fixed animals (8–14 weeks old) through thinned skulls 14–21 d (or 5–6 weeks when noted) after viral injection. Animals were kept warm with a portable heating pad and a local anesthetic (bupivacaine, 0.5%) was applied to the incision areas. Sensory evoked responses were acquired with a Leica M205FA microscope at 6× magnification, a GFP filter set and a Leica FL6000 fluorescence light source. Optical signals were recorded for 9 s per trial at a 464 × 346 pixel resolution. A CCD camera (DFC360 FX, Leica) captured images at a frame rate of 10 Hz and videos were digitized at 12 bits using Leica Application Suite software. Odorants were presented using a custom-made olfactometer (stimulus duration, 3 s) and were presented as ~1% saturated vapor, adjusted for vapor pressure. Separate lines for each odorant were used to prevent cross contamination. The odors were presented in a random order with at least three trials per odorant at interstimulus intervals ≥60 s.

For *in vivo* two-photon calcium imaging, anesthetized mice (IP urethane 1.2 μg/kg) were placed in a stereotaxic head holder (Kopf Instruments) and the temperature of the mouse was maintained between 36.5°C and 37.5°C using a homeothermic blanket system (Harvard Instruments). In the surgical procedure, part of the skin over the skull was resected, the wound margins were sealed with surgical glue (VetBond, 3M) and a head holder was secured to the skull using bone cement. Using a dental drill and carbide bur FG 1/2, a craniotomy was performed over one or both olfactory bulbs, and the exposed tissue was washed with buffer (125 mM NaCl, 5 mM KCl, 10 mM glucose, 10 mM HEPES, 2 mM $CaCl_2$, 2 mM $MgSO_4$, pH 7.4). In most animals the dura was removed, and the window was then sealed using a glass coverslip secured with a thin layer of surgical glue (VetBond, 3M).

We recorded calcium traces using a two-photon resonant microscope (Thorlabs) equipped with a Chameleon Ti-sapphire laser (Coherent) tuned to 920 nm and a 25×, 1.1 NA Nikon objective. The average power output of the objective was kept at less than 150 mW, and calcium activity was typically sampled at ~12 Hz. We recorded data from depths of 180–450 μm below the cortical surface. We used the following odors: pentanol, anisole, acetophenone, isoamyl acetate and a mixture containing the previous odors plus cineol, isobutyric acid, methyl salicylate and (+)-carvone, diluted in mineral oil to approximately 1%, adjusting the single odors for vapor pressure. To deliver odorants, we used a custom-built automated eight-channel olfactometer in which the flow of each odor vial was coupled to a solenoid valve (Lee Company). The experiment was controlled by a custom state system written in LabView (National Instruments). Odorants were presented pseudorandomly for 4 s with 10 s of air flow in between. Each odor was presented between three and six times.

Naris occlusion

We performed reversible, unilateral naris occlusion as previously described[41]. Briefly we constructed removable nose plugs from a small tapered piece of polyethylene tubing (PE-50/10 Warner Instruments) filled with a knotted piece of 3-0 suture silk with an attached hair for easy removal. Nose plugs were randomly inserted into either the right or left nostril of a mouse immediately after viral injection to label granule cells. Nose plugs were left in for 5–6 weeks and inspected every 2 d to ensure consistent occlusion. Animals with early

nose plug removal were not imaged. During calcium imaging, the right bulb was always imaged first.

Olfactory associative learning training

Mice were water-restricted to no less than 85% of their baseline weight beginning 2 d before preliminary training. Water was restricted to 40 mL per kg, per day during the restriction period. Mice were randomly divided into control or training groups. For the training group, mice were trained using a Go/NoGo paradigm in a behavioral chamber with infrared nose pokes (Med Associates Inc.). All mice were first trained to poke their nose into the odor port for at least 300 ms, before moving to the side water port to retrieve water reward within 5 s. After preliminary training sessions (~30–60 min/d for ~5–6 d) mice received viral injections to label cells. After recovery for 2 d, training group mice were trained to respond to the Go odor stimulus (S+) (1% anisole in mineral oil for Fig. 8, 1% acetophenone in mineral oil for Supplementary Fig. 6) by moving to the water port for a reward and were trained to respond to the NoGo odor stimulus[48] (1% pentanol in mineral oil for Fig. 8, 1% (+)-carvone in mineral oil for Supplementary Fig. 6) by refraining from poking into reward ports and starting a new trial. The mice needed to sample the odors for at least 100 ms before responding and to respond within 5 s after odor port poking. False positives (incorrect NoGo response) caused a 4 s timeout punishment. Go and NoGo stimuli were presented to the mice in random sequences during training. Mice were trained for 20 trials per block and ~20 blocks per day. After 3–6 d of odor training, the mice performed at over 80% correct responses. Odors were then diluted with mineral oil to 0.1% and 0.01% to keep the mice actively learning until calcium imaging, which occurred 14–21 d after viral injection and subsequent training. Control mice were still water-restricted, but without associative learning training.

For passive odor exposure, tea balls containing 100 μL of 1% of either pentanol or anisole were hung from the lid of the home cage for exposed mice, or 100 μL of pure mineral oil for control mice, for 1 h per day for 14–21 d after viral labeling until wide-field calcium imaging occurred.

Data analysis

For wide-field calcium imaging, all data analysis was performed with custom written Matlab scripts, which are available upon request. Initial data processing included averaging trials and visually aligning the region of interest (dorsal olfactory bulb). ΔF maps were created by temporally averaging the entire 3-s odor stimulation period and subtracting the temporal average of the 2 s immediately preceding odor onset. $\Delta F/F$ maps were additionally normalized by the first five frames of the averaged trial. There was no appreciable photobleaching of the GCaMP6m signals during the experiments. For quantification, the maps thresholds were set at 50% of the maximum ΔF (or $\Delta F/F$). To generate consensus maps, individual response maps were aligned across preparations, normalized to percent maximal change and then averaged. After averaging, each odor map thresholded odor map was set at 50% maximal amplitude and further smoothed with a mean filter, and the area outline was defined.

For two-photon data processing, all analysis was performed in Matlab (MathWorks). We compensated for motion artifacts in the horizontal plane, and cell detection was done by either detecting circular regions based on minimum diameter, cell contrast, edge sharpness and maximum number of cells per site, with supervision and correction if necessary, or performed entirely manually. Calcium traces were averaged from all pixels in segmented cells and were normalized to $\Delta F/F$. To estimate the responses to olfactory cues, we averaged the calcium activity over the first 3 s following odor onset and subtracted from that the average calcium activity over the last 1 s just before odor onset. Cells were classified as responsive if a *t*-test against 0 proved significant ($P < 0.05$).

Statistics

All data are presented as individual points with bars at mean ± s.e.m. or ± s.d. as indicated. No estimates of statistical power were performed before experiments; animal numbers were minimized to conform to ethical guidelines while accurately measuring neuronal and network responses, and our sample sizes are similar to those reported in previous publications[31,33,40]. Statistical analysis was performed using GraphPad Prism 6 software (GraphPad Software, Inc.), noting the variance to ensure proper statistical parameters were applied. Data distribution was assumed to be normal but this was not formally tested. Statistical methods used include two-tailed students *t*-test with Welch's correction as applicable, one-way ANOVA with Sidak's correction for multiple comparisons, two-way ANOVA or Kolmogorov–Smirnov test as indicated. All histology and electrophysiology analysis were performed blinded. Naris occlusion experiments were performed and analyzed blinded to occluded side. Data collection and analysis for imaging experiments were not performed blind to the conditions of the experiment, but the data were batch processed in Matlab. One Dlx5/6 trained and one Dlx5/6 control animal were excluded due to images being out of focus and one mature Dlx5/6 neuron for the optogenetic mapping experiment was excluded for membrane properties not consistent with granule cells ($C_m > 24$ pF and $R_m < 400$ MΩ).

A Supplementary methods checklist is available.

Data and code availability

The data that support the findings of this study and code are available from the corresponding author upon reasonable request.

Supplementary Material

Refer to Web version on PubMed Central for supplementary material.

Acknowledgments

We would like to thank A. Herman, C. Kim, H. Lu, D. Murphey, K. Schulze and R. Sillitoe for discussion and critical input on this manuscript. This work was supported by the McNair Medical Institute, the Charif Souki Fund, IRACDA Fellowship K12 GM084897 to K.Q., NRSA F31NS089178 to K.U., NINDS grant F31NS081805 to I.G., NINDS R01NS078294 to B.R.A., U54HD083092 to the BCM IDDRC, and the Intelligence Advanced Research Projects Activity (IARPA) via Department of Interior/Interior Business Center (DoI/IBC) contract number D16PC00003 to A.S.T. The US Government is authorized to reproduce and distribute reprints for Governmental purposes notwithstanding any copyright annotation thereon. Disclaimer: The views and conclusions contained

herein are those of the authors and should not be interpreted as necessarily representing the official policies or endorsements, either expressed or implied, of IARPA, DoI/IBC or the US Government.

References

1. Markram H, et al. Interneurons of the neocortical inhibitory system. Nat Rev Neurosci. 2004; 5:793–807. [PubMed: 15378039]
2. Cang J, Feldheim DA. Developmental mechanisms of topographic map formation and alignment. Annu Rev Neurosci. 2013; 36:51–77. [PubMed: 23642132]
3. Iwasato T, et al. NMDA receptor-dependent refinement of somatotopic maps. Neuron. 1997; 19:1201–1210. [PubMed: 9427244]
4. Gordon JA, Stryker MP. Experience-dependent plasticity of binocular responses in the primary visual cortex of the mouse. J Neurosci. 1996; 16:3274–3286. [PubMed: 8627365]
5. Ackman JB, Burbridge TJ, Crair MC. Retinal waves coordinate patterned activity throughout the developing visual system. Nature. 2012; 490:219–225. [PubMed: 23060192]
6. Kakizawa S, Yamasaki M, Watanabe M, Kano M. Critical period for activity-dependent synapse elimination in developing cerebellum. J Neurosci. 2000; 20:4954–4961. [PubMed: 10864953]
7. White JJ, et al. Cerebellar zonal patterning relies on Purkinje cell neurotransmission. J Neurosci. 2014; 34:8231–8245. [PubMed: 24920627]
8. Thivierge JP, Marcus GF. The topographic brain: from neural connectivity to cognition. Trends Neurosci. 2007; 30:251–259. [PubMed: 17462748]
9. Taniguchi H, et al. A resource of Cre driver lines for genetic targeting of GABAergic neurons in cerebral cortex. Neuron. 2011; 71:995–1013. [PubMed: 21943598]
10. Murphey DK, Herman AM, Arenkiel BR. Dissecting inhibitory brain circuits with genetically-targeted technologies. Front Neural Circuits. 2014; 8:124. [PubMed: 25368555]
11. Sohya K, Kameyama K, Yanagawa Y, Obata K, Tsumoto T. GABAergic neurons are less selective to stimulus orientation than excitatory neurons in layer II/III of visual cortex, as revealed by in vivo functional Ca^{2+} imaging in transgenic mice. J Neurosci. 2007; 27:2145–2149. [PubMed: 17314309]
12. Kerlin AM, Andermann ML, Berezovskii VK, Reid RC. Broadly tuned response properties of diverse inhibitory neuron subtypes in mouse visual cortex. Neuron. 2010; 67:858–871. [PubMed: 20826316]
13. Cazakoff BN, Lau BY, Crump KL, Demmer HS, Shea SD. Broadly tuned and respiration-independent inhibition in the olfactory bulb of awake mice. Nat Neurosci. 2014; 17:569–576. [PubMed: 24584050]
14. Fino E, Yuste R. Dense inhibitory connectivity in neocortex. Neuron. 2011; 69:1188–1203. [PubMed: 21435562]
15. Nusser Z, Kay LM, Laurent G, Homanics GE, Mody I. Disruption of GABAA receptors on GABAergic interneurons leads to increased oscillatory power in the olfactory bulb network. J Neurophysiol. 2001; 86:2823–2833. [PubMed: 11731539]
16. Lagier S, Carleton A, Lledo PM. Interplay between local GABAergic interneurons and relay neurons generates gamma oscillations in the rat olfactory bulb. J Neurosci. 2004; 24:4382–4392. [PubMed: 15128852]
17. Sohal VS, Zhang F, Yizhar O, Deisseroth K. Parvalbumin neurons and gamma rhythms enhance cortical circuit performance. Nature. 2009; 459:698–702. [PubMed: 19396159]
18. Kuhlman SJ, Tring E, Trachtenberg JT. Fast-spiking interneurons have an initial orientation bias that is lost with vision. Nat Neurosci. 2011; 14:1121–1123. [PubMed: 21750548]
19. Ohki K, Chung S, Ch'ng YH, Kara P, Reid RC. Functional imaging with cellular resolution reveals precise micro-architecture in visual cortex. Nature. 2005; 433:597–603. [PubMed: 15660108]
20. Shepherd, GM. The Synaptic Organization of the Brain. 5. Oxford Univ. Press; 2004.
21. Carleton A, Petreanu LT, Lansford R, Alvarez-Buylla A, Lledo PM. Becoming a new neuron in the adult olfactory bulb. Nat Neurosci. 2003; 6:507–518. [PubMed: 12704391]

22. Vassar R, et al. Topographic organization of sensory projections to the olfactory bulb. Cell. 1994; 79:981–991. [PubMed: 8001145]
23. Mombaerts P, et al. Visualizing an olfactory sensory map. Cell. 1996; 87:675–686. [PubMed: 8929536]
24. Belluscio L, Katz LC. Symmetry, stereotypy, and topography of odorant representations in mouse olfactory bulbs. J Neurosci. 2001; 21:2113–2122. [PubMed: 11245695]
25. Isaacson JS, Strowbridge BW. Olfactory reciprocal synapses: dendritic signaling in the CNS. Neuron. 1998; 20:749–761. [PubMed: 9581766]
26. Margrie TW, Sakmann B, Urban NN. Action potential propagation in mitral cell lateral dendrites is decremental and controls recurrent and lateral inhibition in the mammalian olfactory bulb. Proc Natl Acad Sci USA. 2001; 98:319–324. [PubMed: 11120888]
27. Bozza T, McGann JP, Mombaerts P, Wachowiak M. In vivo imaging of neuronal activity by targeted expression of a genetically encoded probe in the mouse. Neuron. 2004; 42:9–21. [PubMed: 15066261]
28. Soucy ER, Albeanu DF, Fantana AL, Murthy VN, Meister M. Precision and diversity in an odor map on the olfactory bulb. Nat Neurosci. 2009; 12:210–220. [PubMed: 19151709]
29. Rubin BD, Katz LC. Optical imaging of odorant representations in the mammalian olfactory bulb. Neuron. 1999; 23:499–511. [PubMed: 10433262]
30. Spors H, Grinvald A. Spatio-temporal dynamics of odor representations in the mammalian olfactory bulb. Neuron. 2002; 34:301–315. [PubMed: 11970871]
31. Wachowiak M, et al. Optical dissection of odor information processing in vivo using GCaMPs expressed in specified cell types of the olfactory bulb. J Neurosci. 2013; 33:5285–5300. [PubMed: 23516293]
32. Kohwi M, et al. A subpopulation of olfactory bulb GABAergic interneurons is derived from Emx1- and Dlx5/6-expressing progenitors. J Neurosci. 2007; 27:6878–6891. [PubMed: 17596436]
33. Garcia I, et al. Local CRH signaling promotes synaptogenesis and circuit integration of adult-born neurons. Dev Cell. 2014; 30:645–659. [PubMed: 25199688]
34. Garcia I, et al. Local corticotropin releasing hormone (CRH) signals to its receptor CRHR during postnatal development of the mouse olfactory bulb. Brain Struct Funct. 2016; 221:1–20.
35. Chen Q, et al. Imaging neural activity using Thy1-GCaMP transgenic mice. Neuron. 2012; 76:297–308. [PubMed: 23083733]
36. Chen TW, et al. Ultrasensitive fluorescent proteins for imaging neuronal activity. Nature. 2013; 499:295–300. [PubMed: 23868258]
37. Shipley MT, Adamek GD. The connections of the mouse olfactory bulb: a study using orthograde and retrograde transport of wheat germ agglutinin conjugated to horseradish peroxidase. Brain Res Bull. 1984; 12:669–688. [PubMed: 6206930]
38. Laaris N, Puche A, Ennis M. Complementary postsynaptic activity patterns elicited in olfactory bulb by stimulation of mitral/tufted and centrifugal fiber inputs to granule cells. J Neurophysiol. 2007; 97:296–306. [PubMed: 17035366]
39. Balu R, Pressler RT, Strowbridge BW. Multiple modes of synaptic excitation of olfactory bulb granule cells. J Neurosci. 2007; 27:5621–5632. [PubMed: 17522307]
40. Huang L, et al. Task learning promotes plasticity of interneuron connectivity maps in the olfactory bulb. J Neurosci. 2016; 36:8856–8871. [PubMed: 27559168]
41. Cummings DM, Henning HE, Brunjes PC. Olfactory bulb recovery after early sensory deprivation. J Neurosci. 1997; 17:7433–7440. [PubMed: 9295389]
42. Shepherd GM, Chen WR, Willhite D, Migliore M, Greer CA. The olfactory granule cell: from classical enigma to central role in olfactory processing. Brain Res Rev. 2007; 55:373–382. [PubMed: 17434592]
43. Hensch TK. Critical period plasticity in local cortical circuits. Nat Rev Neurosci. 2005; 6:877–888. [PubMed: 16261181]
44. Ehrlich I, et al. Amygdala inhibitory circuits and the control of fear memory. Neuron. 2009; 62:757–771. [PubMed: 19555645]

45. Breton-Provencher V, Lemasson M, Peralta MR III, Saghatelyan A. Interneurons produced in adulthood are required for the normal functioning of the olfactory bulb network and for the execution of selected olfactory behaviors. J Neurosci. 2009; 29:15245–15257. [PubMed: 19955377]

46. Moreno MM, et al. Olfactory perceptual learning requires adult neurogenesis. Proc Natl Acad Sci USA. 2009; 106:17980–17985. [PubMed: 19815505]

47. Sakamoto M, et al. Continuous postnatal neurogenesis contributes to formation of the olfactory bulb neural circuits and flexible olfactory associative learning. J Neurosci. 2014; 34:5788–5799. [PubMed: 24760839]

48. Alonso M, et al. Olfactory discrimination learning increases the survival of adult-born neurons in the olfactory bulb. J Neurosci. 2006; 26:10508–10513. [PubMed: 17035535]

49. Mandairon N, et al. Neurogenic correlates of an olfactory discrimination task in the adult olfactory bulb. Eur J Neurosci. 2006; 24:3578–3588. [PubMed: 17229106]

50. Monory K, et al. The endocannabinoid system controls key epileptogenic circuits in the hippocampus. Neuron. 2006; 51:455–466. [PubMed: 16908411]

51. Justice NJ, Yuan ZF, Sawchenko PE, Vale W. Type 1 corticotropin-releasing factor receptor expression reported in BAC transgenic mice: implications for reconciling ligand-receptor mismatch in the central corticotropin-releasing factor system. J Comp Neurol. 2008; 511:479–496. [PubMed: 18853426]

52. Arenkiel BR, et al. In vivo light-induced activation of neural circuitry in transgenic mice expressing channelrhodopsin-2. Neuron. 2007; 54:205–218. [PubMed: 17442243]

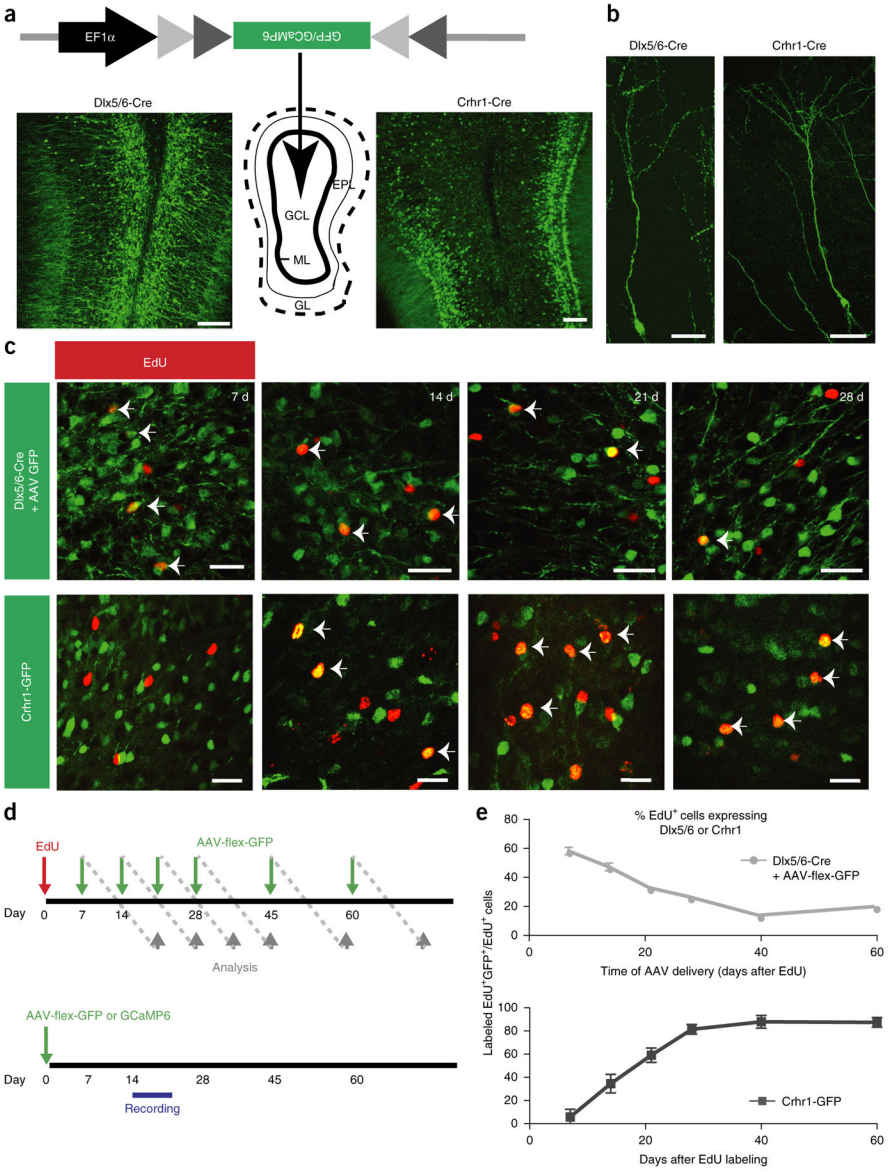

Figure 1.

Genetically targeting populations of granule cells in the adult olfactory bulb. (**a**) Diagram of viral targeting of granule cells showing representative cross-sections from Dlx5/6-Cre (left) and Crhr1-Cre (right) mice labeled with AAV-flex-GFP. GCL, granule cell layer; ML, mitral cell layer; EPL, external plexiform layer; GL, glomerular layer; scale bars, 50 μm. (**b**) Individual granule cells labeled with conditional virus. Scale bars, 25 μm. (**c**) High magnification view of Dlx5/6-Cre AAV-flex-GFP or Crhr1-GFP labeled olfactory bulbs 7, 14, 21 and 28 d after EdU injection. EdU^+GFP^+ cells as a fraction of EdU^+ cells (arrows) decrease with maturation in the Dlx5/6-Cre mice and increase with maturation in the Crhr1-GFP mice. Scale bars, 15 μm. (**d**) Top, timeline of birthdating experiments. Green arrows indicate day of viral injection, when each mouse received a single injection. Gray arrows indicate when labeled animals were killed. Bottom, timeline for imaging and

electrophysiology. Mice received a single injection and then imaging or recording occurred between 14–21 d after viral injection unless otherwise specified. (**e**) Quantification of Dlx5/6 (top) and Crhr1 (bottom, modified from Garcia *et al.*[33]) expression data generated as in **c** in newborn neurons (data points represent averages ± s.e.m., $n = 4$ Dlx5/6-Cre, 3 Crhr1-Cre, 4–6 olfactory bulbs per time point, 5 slices per olfactory bulb).

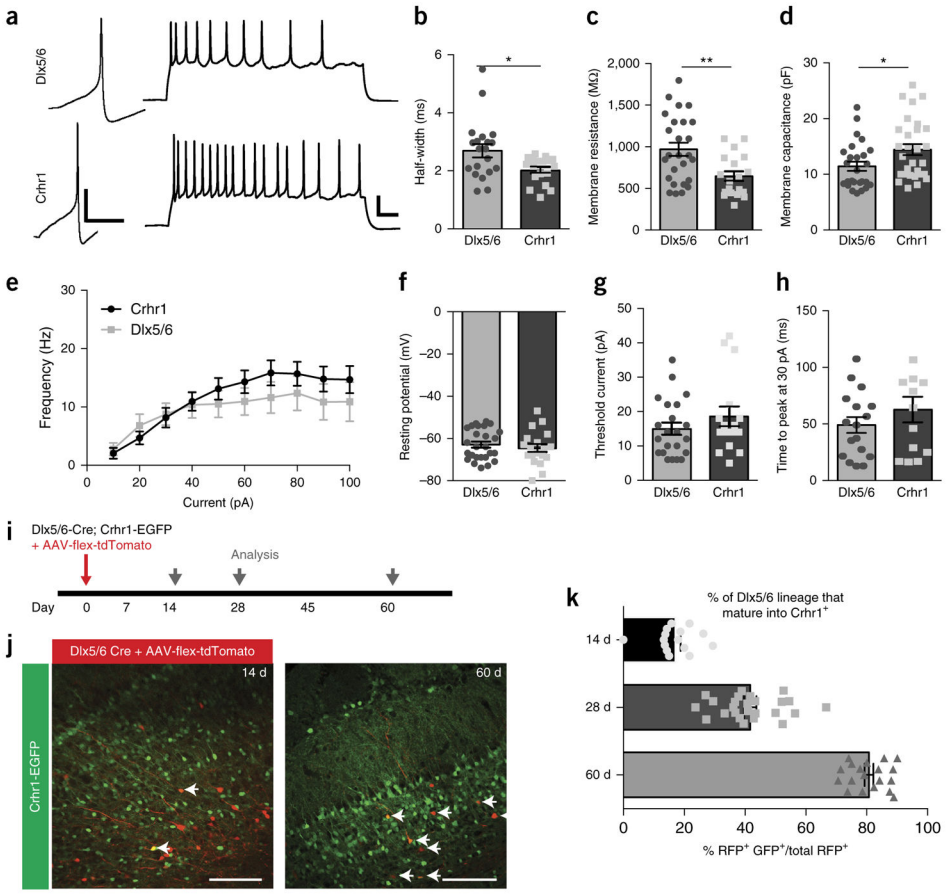

Figure 2.

Comparison of membrane and firing properties of functionally immature Dlx5/6 versus functionally mature Crhr1 granule cells. (**a**) Left, single action potentials in Dlx5/6-Cre AAV-flex-GFP$^+$ neurons (top) and Crhr1-Cre AAV-flex-GFP$^+$ neurons (bottom) at threshold current (10 pA). Scale bars 20 mV, 50 ms. Right, train of action potentials in response to 1 s of 50 pA current injection in Dlx5/6-expressing (top) and Crhr1-expressing (bottom) neurons at threshold current. Scale bars 20 mV, 50 ms. (**b**) Half-widths of action potentials in the immature Dlx5/6-expressing neurons are significantly larger than in the more mature Crhr1-expressing neurons (two-tailed *t*-test, Welch's correction, $*P = 0.0129$, $t = 2.66$, d.f. = 27). (**c**,**d**) Membrane resistances of Dlx5/6-expressing neurons (**c**) are significantly higher than Crhr1-expressing neurons (two-tailed *t*-test, Welch's correction, $**P = 0.0017$, $t = 3.35$, d.f. = 42), whereas membrane capacitances (**d**) are significantly lower (two-tailed *t*-test, Welch's correction, $*P = 0.0241$, $t = 2.32$, d.f. = 52). (**e**) Frequency–current curves for the two populations of granule cells for average number of spikes after 1 s depolarizing current injections (10 pA steps). (**f**–**h**) There was no change in the resting potential (**f**) (two-tailed *t*-test, Welch's correction, $P = 0.4493$, $t = 0.76$, d.f. = 36), current required to fire and action potential from resting potential (**g**) (two-tailed *t*-test, Welch's correction, $P = 0.2889$, $t = 1.083$, d.f. = 26), or time to action potential peak from threshold voltage (**h**) (two-tailed *t*-test, Welch's correction, $P = 0.4493$, $t = 1.025$, d.f. = 21), between Dlx5/6 and Crhr1-expressing neurons. (**i**) Experimental time line to determine when immature Dlx5/6-

expressing neurons begin to express CHRH. (**j**,**k**) Example images (**j**) of Dlx5/6-Cre;Crhr1-GFP bulbs injected with AAV-flex-tdTomato at 14 d (left) and 60 d (right) after injection, with data quantification (**k**). Scale bars, 100 μm. Data points represent averages ± s.e.m.; for electrophysiology (**a**–**h**), n = 26 Dlx5/6 cells from 7 mice, n = 19 Crhr1 cells from 6 mice; for staining (**j**,**k**), n = 4 bulbs, 3–5 slices per bulb, per time point.

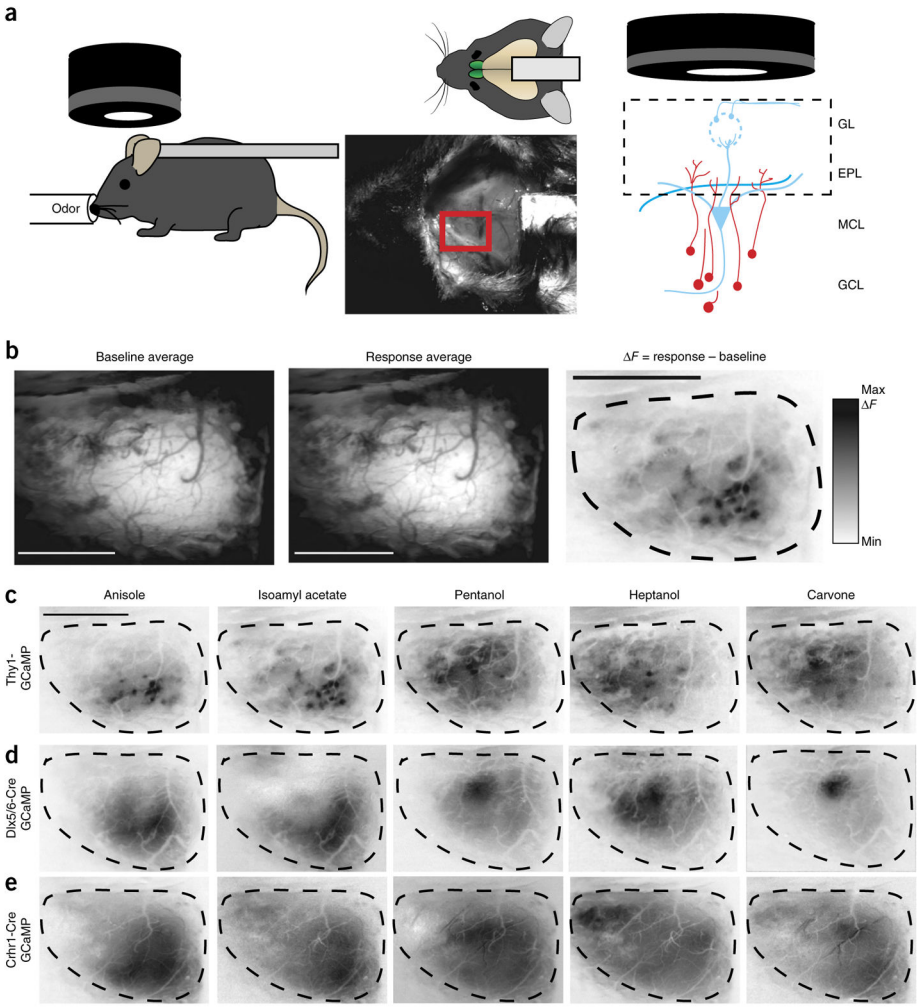

Figure 3.

Olfactory sensory maps from different populations of olfactory bulb neurons visualized through calcium imaging. (**a**) *In vivo* imaging of entire dorsal olfactory bulb surface (red rectangle) in anesthetized, head-fixed mice. Epifluorescence detects intensity changes of GCaMP-expressing dendrites in the olfactory bulb (right). GCL, granule cell layer; MCL, mitral cell layer; EPL, external plexiform layer; GL. glomerular layer. (**b**) Olfactory response sensory maps (right) are created from averaging across 3 trials (top left) per animal and then subtracting the temporal average of the baseline fluorescence (left) from the response average (middle). Scale bars, 1 mm. (**c**–**e**) Example response maps to five different odorants; scale bar, 1 mm. (**c**) Response maps (as in **b**) for a Thy1-GCaMP3 mouse shows mitral and tufted cell dendrite activation displaying glomerular activation patterns. Immature (**d**) and mature (**e**) granule cell maps, in a Dlx5/6-Cre AAV-flex-GCaMP6 mouse and a Crhr1-Cre AAV-flex-GCaMP6 mouse, respectively, show more diffuse odor-dependent areas of activation.

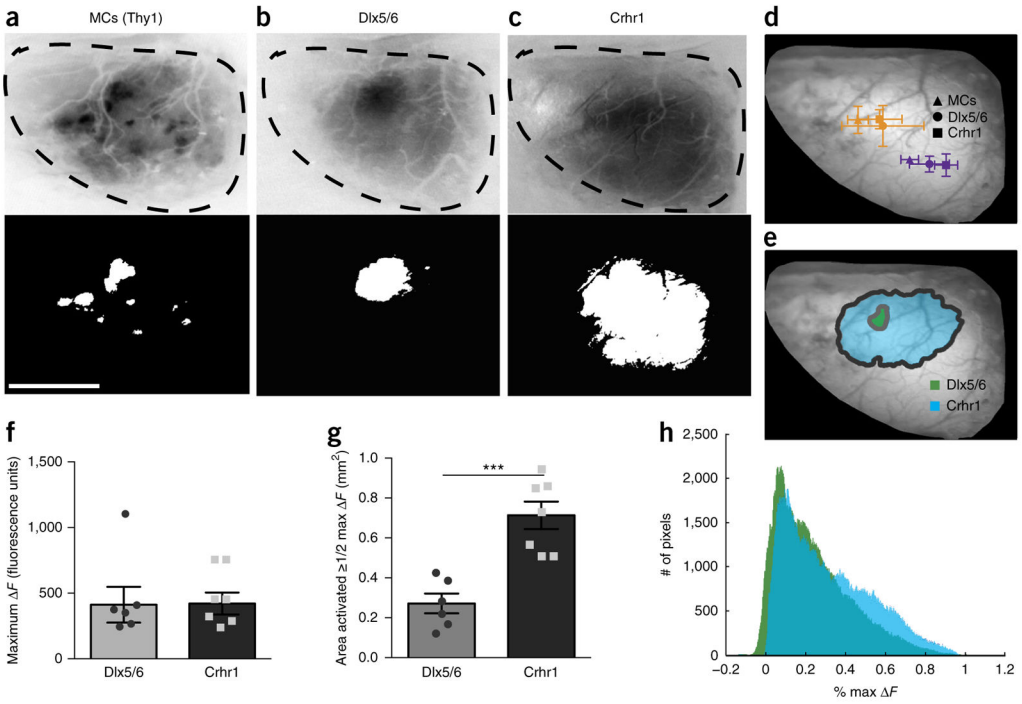

Figure 4.

Inhibitory sensory maps broaden with maturation. (**a**–**c**) Example sensory map for pentanol (top) and the area activated at 50% or more of the maximal change in fluorescence (50% maximal Δ*F*) (bottom) for mitral cells (MCs) in the Thy1-GCaMP3 (**a**), Dlx5/6-Cre AAV-flex-GCaMP6 (**b**) and Crhr1-Cre AAV-flex-GCaMP6 (**c**) mice. Scale bar, 1 mm. (**d**) Average centroid location of the activated area for pentanol (orange) and anisole (purple) across the different neuronal populations: mitral cells (triangles), immature granule cells (circles) and mature granule cells (squares). (**e**) Consensus maps for all animals of the activated area (see Online Methods). (**f**) No change in maximal Δ*F* value across animals (two-tailed *t*-test, $P = 0.9557$, $t = 0.06$, d.f. = 11). (**g**) Significant increase in the activated area (50% or more of maximal Δ*F*) for the mature granule cells (two-tailed *t*-test, $P = 0.0004$, $t = 5.06$, d.f. = 11). (**h**) Histogram of change in fluorescence intensity values normalized to maximal Δ*F* for all pixels from the pentanol sensory maps. Bars represent averages ± s.d. (**d**) or s.e.m. (**f**,**g**); $n = 6$ animals for Dlx5/6-Cre, $n = 7$ animals for Crhr1-Cre and $n = 4$ animals for Thy1-GCaMP, minimum of 3 trials per odorant.

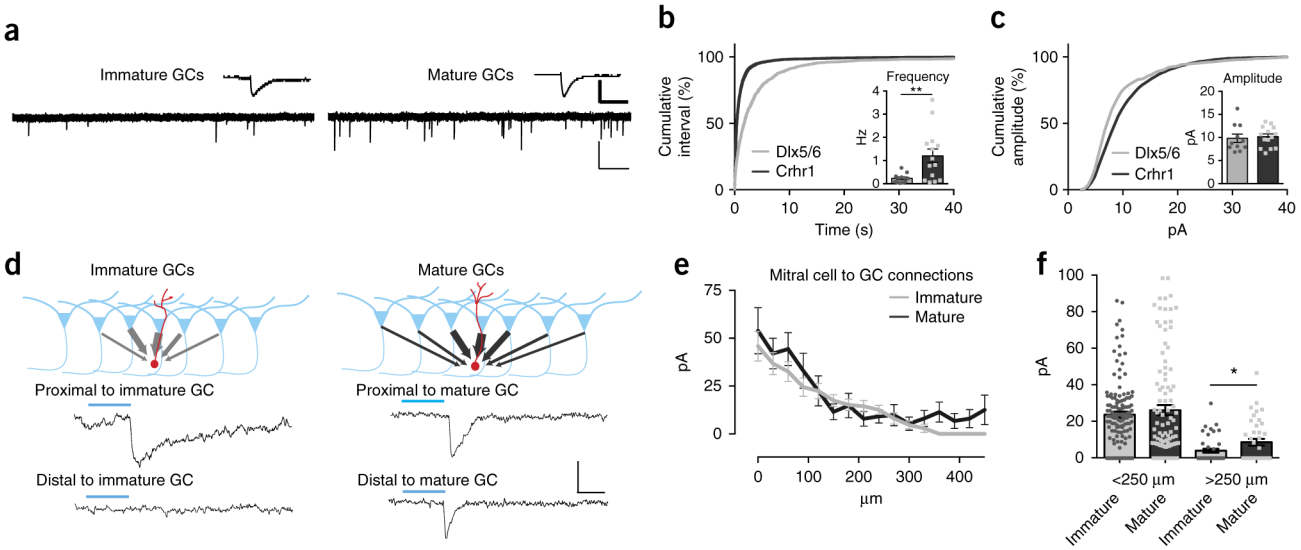

Figure 5.

Mature granule cells show recruitment over refinement of synaptic inputs. (**a**) Representative traces and average event (top insets) of mEPSCs from an immature Dlx5/6-Cre AAV-flex-GFP neuron (left) and a mature Crhr1-Cre AAV-flex-GFP neuron (right). Scale bars: full trace (light bars) 20 pA, 1 s; average (heavy bars) 8 pA, 11 ms. (**b**) Cumulative distribution plot of inter-event interval. mEPSCs are significantly different between Dlx5/6 and Crhr1-expressing neurons (KS test, $P < 0.0001$, $D = 0.36$). Inset: mean frequency of mEPSCs from immature Dlx5/6 and mature Crhr1 granule cells (two-sided *t*-test, Welch's correction, $P = 0.0065$, $t = 3.20$, d.f. = 13). (**c**) Cumulative distribution plot. Amplitudes of the mEPSCs are significantly different between Dlx5/6 and Crhr1 neurons (KS test, $P < 0.0001$, $D = 0.16$). Inset: mean amplitude of mEPSCs of immature Dlx5/6 and mature Crhr1 granule cells ($n = 13$ granule cells from 5 Dlx5/6 animals and 11 granule cells from 5 Crhr1 animals). (**d**) Top: optogenetic mapping of mitral cell inputs onto granule cells. Bottom: example traces of laser-evoked excitatory currents onto immature neurons (right, from Thy1-ChR2; Dlx5/6-Cre animals recorded 2–3 weeks after injection) and mature neurons (left, from Thy1-ChR2;Dlx5/6-Cre animals recorded 5–6 weeks after injection), highlighting stimulation of areas either proximal (<250 µm; top) or distal (<250 µm; bottom) to the recorded cell. Scale bars 15 pA, 10 ms. (**e**) Average connection strength as a function of lateral distance from the granule cell. (**f**) Mature granule cells receive stronger input from distal connections (two-sided *t*-test, $* P = 0.0326$, $n = 8$ cells per group). Bar graphs in **b**,**c**,**e**,**f** represent mean values ± s.e.m.

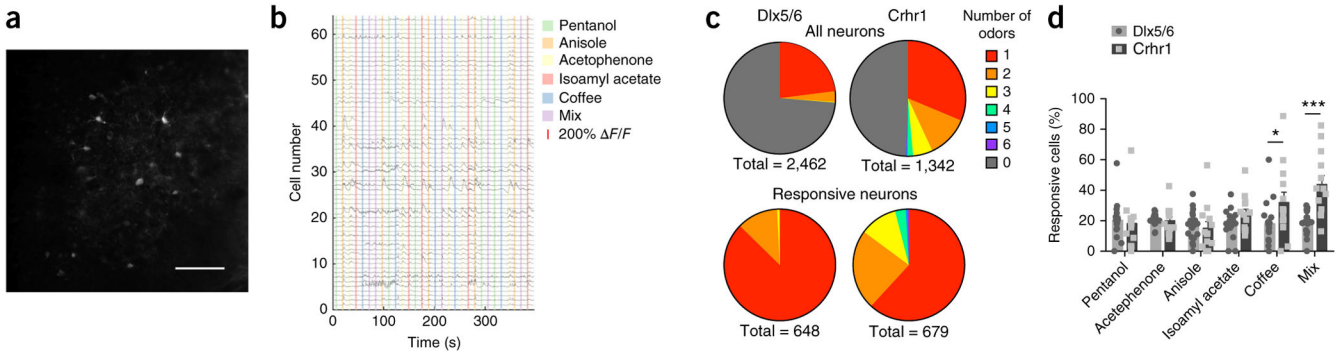

Figure 6.

Individual granule cells respond to more odors with maturation. (**a**) Single frame of *in vivo* two-photon GCaMP signal from Crhr1-expressing cells imaged 350 μm deep. Scale bar, 100 μm. (**b**) Δ*F*/*F* traces from neurons in **a**. (**c**) Number of odorants neurons responsive as a fraction of all imaged neurons within a single plane (top) or as a fraction of responsive neurons within a single plane (bottom). (**d**) Quantification of neurons responding to individual odors as a percentage of cells that responded to any odor (two-way ANOVA, Sidak's multiple comparison correction, $*P = 0.0274$, $t = 2.87$, d.f. = 174; $***P < 0.0001$, $t = 5.06$, d.f. = 174). Bars are mean percent per imaging plane ± s.e.m., 2–5 planes per animal, 3 animals each genotype injected with AAV-flex-GCaMP6 virus and imaged 2–3 weeks after injection.

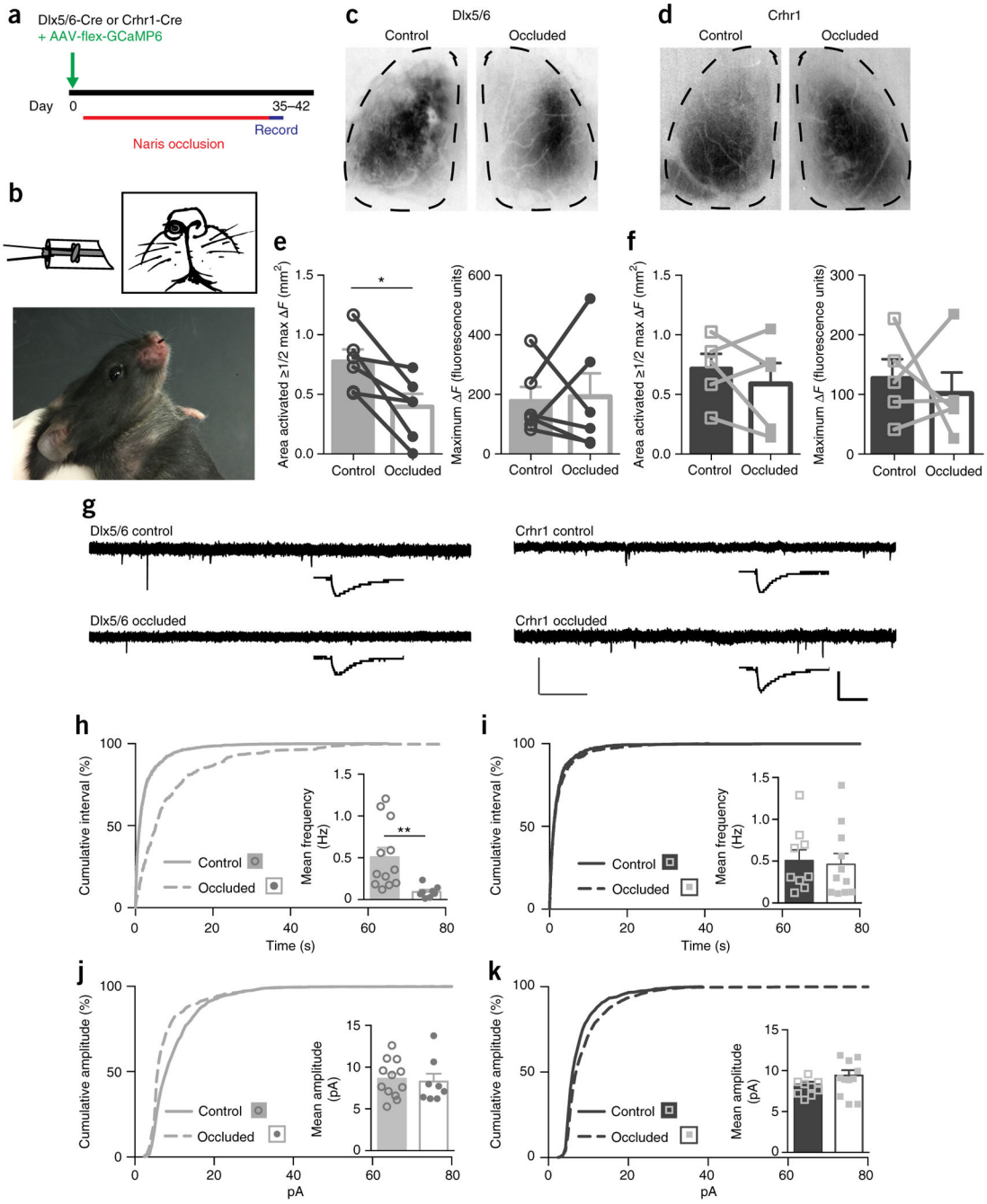

Figure 7.

Decreased sensory experience prevents sensory map expansion. (**a**) Timeline for removable unilateral naris occlusion experiments. (**b**) Diagram of the nose plug as described by Cummings *et al.*[41], made from polyethylene tubing, and photo of inserted nose plug. (**c**–**f**) Naris occlusion prevents expansion of the area activated (to 50% or more of max Δ*F*) in the immature (Dlx5/6-Cre AAV-flex-GCaMP6) cells (**c**, quantified in **e**; two-tailed paired *t*-test, $P = 0.0111$, $t = 2.90$, d.f. = 15), but does not change the activated area of the mature (Crhr1+ AAV-flex-GCaMP6) cells (**d**, quantified in **f**; two-tailed *t*-test, $P = 0.4236$, $t = 0.89$, d.f. = 5).

Naris occlusion does not change the maximal ΔF for either maturation state (**e**,**f**). Data points represent the occluded or control bulb from individual animals; bars show mean values ± s.e.m. (**g**) Representative traces of mEPSC recordings from Dlx5/6 (left) and Crhr1 (right) granule cells after 5–6 weeks of naris occlusion in control or occluded bulbs. Scale bars: full trace (light bars) 20 pA, 1 s; average (heavy bars) 8 pA, 10 ms. (**h**,**i**) Cumulative distribution of inter-event interval of the mEPSCs are significantly different for the Dlx5/6-expressing cells (KS test, $P < 0.0001$, $D = 0.45$). Insets: mean frequency of mEPSCs of immature Dlx5/6-expressing and mature Crhr1-expressing granule cells (two-sided *t*-test, Welch's correction, $^{**}P = 0.0038$, $t = 3.58$, d.f. = 12). (**j**,**k**) Cumulative distributions of amplitude of the mEPSCs are significantly different for the two types (KS test, **j**: $P < 0.0001$, $D = 0.23$, **k**: $P < 0.0001$, $D = 0.12$). Inset: mean amplitude of mEPSCs of immature Dlx5/6 and mature Crhr1 granule cells. Bar graphs in **h**–**k** represent mean values ± s.e.m.; for mEPSC data: $n = 13$ control granule cells and 8 occluded cells from 4 animals for Dlx5/6 and $n = 12$ control granule cells and 11 occluded from 4 animals for Crhr1.

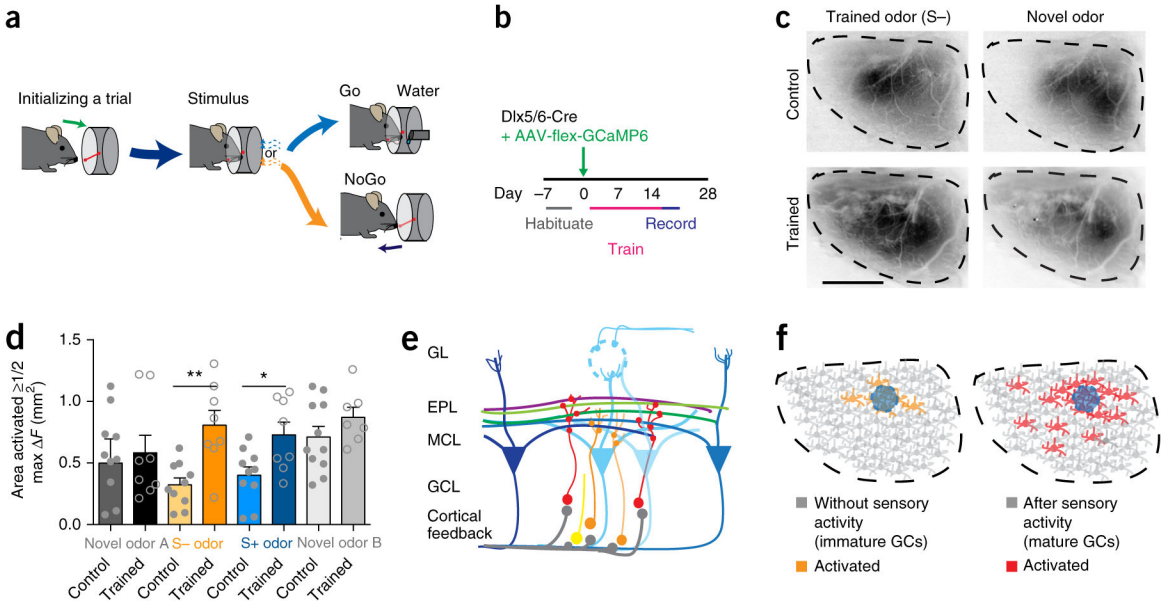

Figure 8.

Olfactory learning precociously expands inhibitory sensory maps. (**a**) Timeline and (**b**) experimental set up for the Go/No Go odor learning task. (**c**) Representative Δ*F* sensory map from Dlx5/6-Cre AAV-flex-GCaMP6 control and trained mice in response to the unrewarded trained odor (pentanol; S−) and a novel odor (acetophenone). Scale bar, 1 mm. (**d**) After training, the activated area (50% or more of max Δ*F*) is significantly increased for the training-associated rewarded (S+) and unrewarded (S−) odors but not novel odors (one-way ANOVA, Sidak's multiple correction, $*P = 0.0493$, $t = 2.31$, d.f. = 48; $**P = 0.0028$, $t = 3.40$, d.f. = 48; bars represent mean values ± s.e.m., $n = 8$ animals trained, 10 animals control). (**e**) Diagram of lateral dendrites from mitral cells activated by distant glomeruli synapsing (red circles) with mature granule cells (red) while immature granule cells (orange) receive fewer synapses (orange circles) from local cortical or proximal mitral cell synapses. (**f**) Model of activated granule cells (GCs) in animals with immature or minimal sensory experience (left) and mature or increased sensory experience (right). Colored neurons are activated by the same stimulus, which also activates the nearby glomerulus (blue circle).